Journal of Biomedical Optics

SPIEDigitalLibrary.org/jbo

Analysis of mechanical contrast in optical coherence elastography

Kelsey M. Kennedy
Chris Ford
Brendan F. Kennedy
Mark B. Bush
David D. Sampson

SPIE

Analysis of mechanical contrast in optical coherence elastography

Kelsey M. Kennedy,[a] Chris Ford,[b] Brendan F. Kennedy,[a] Mark B. Bush,[c] and David D. Sampson[a,d]
[a]University of Western Australia, Optical+Biomedical Engineering Laboratory, 35 Stirling Highway, Crawley, Western Australia 6009, Australia
[b]Curtin University, Department of Mechanical Engineering, Perth, Western Australia 6102, Australia
[c]University of Western Australia, School of Mechanical and Chemical Engineering, 35 Stirling Highway, Crawley, Western Australia 6009, Australia
[d]University of Western Australia, Centre for Microscopy, Characterization and Analysis, 35 Stirling Highway, Crawley, Western Australia 6009, Australia

Abstract. Optical coherence elastography (OCE) maps the mechanical properties of tissue microstructure and has potential applications in both fundamental investigations of biomechanics and clinical medicine. We report the first analysis of contrast in OCE, including evaluation of the accuracy with which OCE images (elastograms) represent mechanical properties and the sensitivity of OCE to mechanical contrast within a sample. Using phase-sensitive compression OCE, we generate elastograms of tissue-mimicking phantoms with known mechanical properties and identify limitations on contrast imposed by sample mechanics and the imaging system, including signal-processing parameters. We also generate simulated elastograms using finite element models to perform mechanical analysis in the absence of imaging system noise. In both experiments and simulations, we illustrate artifacts that degrade elastogram accuracy, depending on sample geometry, elasticity contrast between features, and surface conditions. We experimentally demonstrate sensitivity to features with elasticity contrast as small as 1.1:1 and calculate, based on our imaging system parameters, a theoretical maximum sensitivity to elasticity contrast of 1.002:1. The results highlight the microstrain sensitivity of compression OCE, at a spatial resolution of tens of micrometers, suggesting its potential for the detection of minute changes in elasticity within heterogeneous tissue. [DOI: 10.1117/1.JBO.18.12.121508]

Keywords: optical coherence tomography; elastography; mechanical properties; finite element modeling; tissue phantoms.

Paper 130458SSR received Jul. 2, 2013; revised manuscript received Sep. 20, 2013; accepted for publication Oct. 14, 2013; published online Nov. 12, 2013.

1 Introduction

When tissue becomes diseased, it undergoes changes in its constituent materials and microstructure, which translates to changes in its mechanical properties.[1] Optical coherence elastography (OCE)[2] is an emerging imaging technique that probes mechanical contrast on a microscale. To perform OCE, a mechanical load is applied to tissue, and optical coherence tomography (OCT) is used to measure the resulting displacements, from which variations in elasticity, or stiffness, are estimated and mapped into an image known as an elastogram. OCE probes mechanical contrast on a length scale (tens of micrometers) considerably smaller than that probed by other elastography techniques, such as ultrasound (hundreds of micrometers)[3] and MRI (~1 mm).[4] It also provides a depth-resolved capability, unlike cellular-scale and nanoscale elasticity mapping techniques such as atomic force microscopy[5] and optical tweezers.[6] As this unique length scale is relevant to the progression of many diseases, OCE has the potential to become a valuable tool for imaging of tissue microarchitecture, with possible applications ranging from fundamental studies of biomechanics to numerous aspects of clinical medicine. So far, OCE has been proposed for a number of clinical applications, such as assessing the vulnerability of atherosclerotic plaques,[7,8] guiding surgical resection of soft tissue tumors,[9] and monitoring changes in corneal elasticity with age and progression of disease.[10–12]

A number of techniques have been proposed to date for performing OCE and may be grouped according to the type of loading used. The first reported technique is compression OCE, in which a compressive load is applied to a sample, and the resulting strain is estimated and mapped into a strain elastogram.[2,13–18] Strain provides a relative measure of elasticity under the assumption of a uniform stress field within the sample. More recently, shear wave and surface wave techniques have been proposed, which measure the phase velocity of a propagating wave generated using either vibration or impulse loading.[19–22] Unlike compression OCE, such methods directly estimate sample elasticity. However, compression OCE maintains the native lateral resolution of the OCT system, whereas shear and surface wave techniques have considerably lower lateral resolution (0.5 to 1 mm), as they assume tissue homogeneity for the length over which the shear wave speed is calculated. Compression elastography is also straightforward to implement and has been extensively used for clinical imaging in ultrasound elastography.[23] In addition to compression and shear/surface wave OCE, techniques have been proposed that use internal, localized loading generated by a magnetic implant[24] or by magnetic nanoparticles embedded in the sample.[25]

A variety of methods for measuring displacement using OCT have also been proposed, including speckle tracking,[2] phase-sensitive OCE,[26] and use of the Doppler spectrum.[27]

Address all correspondence to: Kelsey M. Kennedy, University of Western Australia, School of Electrical, Electronic & Computer Engineering (M018), Optical+Biomedical Engineering Laboratory, 35 Stirling Highway, Crawley, Western Australia 6009, Australia. Tel: +61 8 6488 3916; Fax: +61864881319; E-mail: 20413465@student.uwa.edu.au

0091-3286/2013/$25.00

Despite the breadth of the proposed techniques and potential clinical applications, the limitations on mechanical contrast that can be detected in OCE elastograms remain poorly understood. The contrast in elastograms is determined by a combination of the true elasticity distribution within the tissue, the employed imaging system parameters, and the assumptions made about tissue behavior in the elastogram reconstruction process. To better understand the ability of OCE to detect mechanical contrast in tissue and to enable more useful interpretation of OCE elastograms, some fundamental questions must be addressed:

1. How accurately do OCE elastograms represent the elasticity distribution within a sample?
2. What is the sensitivity of OCE elastograms to variations in elasticity within a sample?
3. What factors limit elastogram accuracy and sensitivity?

In this article, we address these questions in the context of phase-sensitive compression OCE. We present strain elastograms of tissue-mimicking phantoms with varying geometries and a range of mechanical contrast between features and identify limitations on elastogram contrast imposed by built-in aspects of tissue mechanics. We focus our analysis on the detection of features within mechanically heterogeneous samples, as this aspect is the most relevant for assessing the ability of OCE to differentiate normal versus diseased or compromised regions within biological tissue. Thus, relative, rather than absolute, measurements of elasticity are the focus of our analysis.

We employ finite element models (FEMs) in this study to generate simulated elastograms and analyze the impact of varying mechanical parameters on contrast, independent of imaging system noise and signal processing techniques. We also use FEMs to test the validity of assumptions made about sample behavior in the elastogram formation process and to analyze how the breakdown of these assumptions impacts on elastogram accuracy.

We, then, consider how elastogram contrast is limited by imaging system and signal processing parameters and quantify the sensitivity and range of mechanical contrast achievable using our compression OCE system. In so doing, we keep the imaging and signal processing parameters constant throughout this study, as our objective is to investigate the impact of varying mechanical parameters, and how the fundamental mechanics combine with the imaging system capabilities to determine contrast.

2 Compression OCE

In this section, we describe the deformation of a sample undergoing compression, highlight the assumptions made about tissue mechanical behavior in the elastogram formation process, and describe how elastogram accuracy may be measured. We also define expressions for measures of elastogram quality in phase-sensitive compression OCE, including resolution, sensitivity, and dynamic range (DR).

2.1 *Tissue Deformation in Compression Elastography*

A compressive load applied to a sample is described in terms of stress, $\sigma = F/A$, where F is the applied force and A is the cross-sectional area over which the force is applied. The resulting bulk deformation of the sample along the axis of compression is quantified by strain, $\varepsilon = \Delta l/l_0$, where Δl is the change in length and l_0 is the original length of the sample. The axial compression of a sample is generally accompanied by some lateral expansion, to conserve volume. This shape change is characterized by Poisson's ratio, υ, which is equal to 0.5 for a completely incompressible material and commonly assumed to be in the range ~0.49 to 0.5 for most soft tissues.[28]

If we make the assumption that tissue deforms in a linearly elastic manner, which has been reported to be an accurate approximation for strains <0.1 in tissues such as breast and prostate,[29] stress and strain are related through a three-dimensional (3-D) set of elastic constants. In compression elastography, the applied load can be approximated as uniaxial, i.e., occurring along one axis of the sample. Under the further assumption that the sample is isotropic, i.e., its response to stress is direction independent, the uniaxial stress and strain are related through one elastic constant, defined as the Young's modulus, $E = \sigma/\varepsilon$. The Young's modulus is commonly used to characterize the elasticity of tissues and, for soft tissues, has been reported to range from hundreds of Pascals (Pa) for healthy liver tissue,[30] to tens and hundreds of kilopascals for healthy and malignant breast tissues,[29] to a few megapascals for arterial wall tissues.[31]

The objective of compression OCE is to form a map of Young's modulus within the sample—a so-called elastogram. The equation for Young's modulus given above describes a "bulk" response of a sample, but a map of Young's modulus requires knowledge of the "local" stresses and strains throughout the sample. Local strain is obtained by calculating the spatial derivative of the measured displacement, i.e., the change in displacement per unit length of the sample. Local stress, on the other hand, cannot be directly measured at depth within the sample. As a result, the elastogram in compression OCE is typically a map of strain, which gives a relative measure of Young's modulus, under the assumption that stress is uniformly distributed throughout the sample. However, in practice, stress concentrations arise at feature boundaries within heterogeneous samples[32] and at the sample surface where friction is present. Thus, strain elastograms are subject to mechanical artifacts that limit their accuracy in representing the true elasticity distribution in a sample.

2.2 *Quantification of Elastogram Accuracy*

A measure of elastogram accuracy (fidelity to the true elasticity distribution) is the contrast transfer efficiency (CTE), which was defined by Ponnekanti et al.[32] in ultrasound elastography as the ratio of strain contrast observed between features in an elastogram, C_o, to true elasticity contrast of the features, C_t: CTE $= C_o/C_t$. We employ this definition of CTE to quantify elastogram accuracy in this article and address the first question in the introduction: "How accurately do OCE elastograms represent the elasticity distribution in a sample?"

In compression elastography, the CTE of strain elastograms depends on the validity of the assumption of uniform distribution of stress. This assumption holds for the trivial case of a mechanically homogeneous sample undergoing uniaxial compression, which results in a uniform strain field but provides no elasticity information without a measurement of the applied stress. We consider here the more relevant case of a mechanically heterogeneous sample, in which the aim is to differentiate features based on mechanical contrast within an image. In particular, we consider two heterogeneous sample geometries: bilayer (soft on stiff) and stiff inclusions embedded in a soft matrix. Analytical expressions for the CTE of strain elastograms

have been derived for each of these geometries, assuming an infinite medium of isotropic, linear elastic material undergoing uniaxial compression, in which each material in the structure has equal Poisson's ratio. For a layered structure, by considering an equivalent system of springs, it can be shown that the stress is uniformly distributed among the layers, such that the strain contrast between layers is inversely proportional to the Young's modulus contrast between layers.[33] In other words, a strain elastogram of a layered geometry is expected to have CTE = 1.

Kallel et al.[34] used an analytical solution to the elasticity equations to derive expressions for the CTE of strain elastograms of an inclusion geometry. They found that for the case of an inclusion perfectly embedded (bonded to its surroundings) in a homogeneous matrix material, the contrast between the strain in the inclusion, $\varepsilon_{\text{inclusion}}$, and strain in the matrix, $\varepsilon_{\text{matrix}}$, (at large distances from the inclusion), $C_{\text{o}} = \varepsilon_{\text{inclusion}}/\varepsilon_{\text{matrix}}$, is related to the true modulus contrast between the inclusion and matrix, $C_t = E_{\text{inclusion}}/E_{\text{matrix}}$, by

$$\frac{1}{C_{\text{o}}} = \left[\frac{1-2\upsilon}{C_t+(1-2\upsilon)} + \frac{2}{1+C_t(3-4\upsilon)}\right]. \quad (1)$$

Note that C_{o} depends neither on the size of the inclusion nor on its depth below the surface, but only on the modulus contrast between the inclusion and matrix and on the Poisson's ratio, υ, which, as discussed above, falls in the range ~0.49 to 0.5 for most soft tissues. In this case, Eq. (1) may be approximated as $C_{\text{o}} = 1/2 + C_t/2$. This indicates that for increasing elasticity contrast between a stiff inclusion and a soft matrix, the observed strain contrast is also expected to increase but that the CTE will plateau at just over 0.5 for large modulus contrast.[32,34] This is illustrated and explained in detail in Sec. 4.2. Equation 1 also applies to the case of a soft inclusion embedded in a stiff matrix; however, we limit the analyses in the present study to consider stiff inclusions.

The analysis of elastogram accuracy described above, first introduced in ultrasound elastography, is independent of the spatial resolution scale of the employed elastography technique and so may be applied to compression OCE. A key difference in OCE, however, is an increased sensitivity to surface effects (friction and coupling with the compressor) as images are generally limited by the penetration depth of OCT to the first 1 to 2 mm in dense tissues. Furthermore, optical interferometric detection in OCE will translate to a higher sensitivity to deformation than in ultrasound elastography, and the higher spatial resolution and smaller field of view in OCE will mean that a different scale of tissue structures is probed. We further examine some of these issues in the discussion in Sec. 5.

Finite element modeling is used in this study for addressing mechanical aspects of the third question proposed above: "What factors limit the accuracy and sensitivity?" Once shown to produce results that accurately model the physical system, FEMs enable ready variation of mechanical parameters, including sample geometry, mechanical properties, and surface friction. The model predicts the effects of these parameters on the resulting strain distribution in the absence of imaging system noise. Importantly, FEMs also provide estimates of the resulting stress distribution, allowing identification of sources of mechanical artifacts in strain elastograms.

2.3 *Strain Elastogram Performance Parameters in Compression OCE*

In addition to artifacts arising from built-in aspects of mechanical behavior, elastogram contrast depends on imaging system noise and parameters used in signal processing, particularly in the strain estimation process. Our group recently defined performance parameters for strain elastograms in compression OCE, in terms of the mean and variance of the measured displacement values.[15] Here, we summarize those definitions for reference in this article.

In phase-sensitive OCE, local displacement, $d(z)$, is calculated from the change in phase, $\Delta\phi(z)$, between A-scans or B-scans,[26] scaled by the mean wavelength of the source in the sample, λ/n, where n is the refractive index of the sample, i.e., $d(z) = \Delta\phi(z)\lambda/4\pi n$. The local strain, ε_l, is then estimated as the gradient of displacement over a range in depth: $\varepsilon_l = \Delta d/\Delta z$. In this equation, Δz is the strain resolution, defined as $\Delta z = mdz$, where m is the number of OCT image pixels over which strain is estimated, and dz is the axial pixel size.

The strain sensitivity, S_ε, is defined as the standard deviation of strain (σ_ε) and, in phase-sensitive OCE, depends fundamentally on the phase stability of the OCT system. The strain dynamic range, DR_ε, is defined as the ratio of the maximum strain to the strain sensitivity. In this article, we assume that the maximum detectable strain is that due to a phase change of π radians within one strain resolution (the axial distance over which the strain is estimated). Thus, the maximum measurable displacement, Δd_{max}, is equal to $\lambda/4n$. Under this assumption, the strain DR is defined as

$$\text{DR}_\varepsilon \equiv \frac{\frac{\Delta d_{\text{max}}}{\Delta z}}{\sigma_\varepsilon} = \frac{\lambda}{4n\sigma_\varepsilon\Delta z}. \quad (2)$$

The strain sensitivity and DR, as defined above, in combination with the contrast transfer functions detailed in the previous section, will determine the ultimate sensitivity of OCE strain elastograms to variations in elasticity within a sample. We present an analysis of this sensitivity in Sec. 4.3.

3 Methods

3.1 *Phantom Fabrication and Characterization*

Tissue-mimicking phantoms with controllable structure and mechanical properties were fabricated using a range of silicone elastomers, namely, combinations of Elastosil® RT601, Elastosil® P7676, and AK50 Silicone Fluid (Wacker, Germany).[35] Three types of phantoms were constructed for this study: homogeneous, bilayer, and inclusion. All phantoms were cylindrical with 15-mm diameter and were made ~1 mm thick such that OCT could readily image the entire depth of the phantom to facilitate comparison to the FEM. Representative OCT B-scans of each phantom type are shown in Fig. 1. All OCT images have been scaled to physical dimensions using a refractive index of 1.4 for the silicone materials.[35] The bilayer phantoms comprise two layers (soft and stiff) of approximately equal thickness. The inclusion phantoms consist of a soft silicone matrix containing a stiff silicone inclusion in the form of a rectangular prism embedded 300 to 350 μm below the surface. The inclusions were cut by hand from a bulk of cured silicone to sizes in the range of 300 to 500 μm. This range was set by the

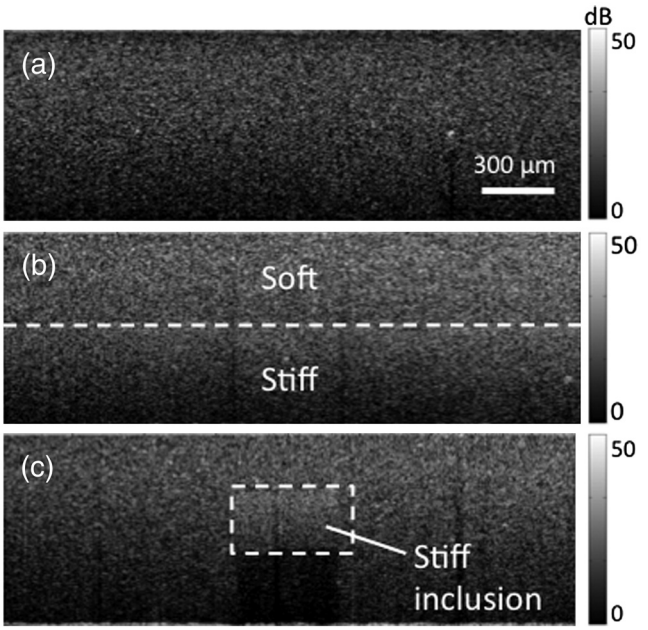

Fig. 1 Optical coherence tomography (OCT) B-scans of (a) homogeneous, (b) bilayer, and (c) inclusion phantoms. Scale bar applies to both dimensions. Dashed lines in (b) and (c) indicate feature boundaries.

achievable tolerances. (Smaller inclusions than those used here could be fabricated using soft lithography techniques previously used to fabricate 3-D structured phantoms.[36]) To ensure that layers and inclusions were distinguishable in OCT images, titanium dioxide particles were added to the uncured silicones in concentrations of 0.8 mg/mL for the homogeneous phantoms, matrix materials, and top layers, and 2.5 mg/mL for the inclusions and bottom layers.

The Young's modulus of the cured silicone was controlled by varying the volumetric ratio of crosslinker, catalyst, and non-crosslinking silicone fluid.[35] To measure the Young's modulus of each silicone, stress–strain curves were obtained using standard compression tests (Instron, Norwood, Massachusetts). The Young's modulus was then estimated by linear regression against the stress-strain curves, as described in further detail in Sec. 3.3.2.

3.2 *Compression OCE System and Measurements*

Compression OCE measurements were performed using a fiber-based, Fourier-domain OCT system. The light source is a superluminescent diode with a central wavelength of 835 nm and bandwidth of 50 nm. The measured axial resolution is 8.5 μm. The lens in the sample arm has a working distance of 25 mm and provided a measured lateral resolution of 11 μm. The measured sensitivity is 102 dB at an exposure time of 36 μs. B-scans were acquired with 1000×2048 $(x \times z)$ pixels over a 6×3 mm field of view and at a line rate of 10 kHz.

The sample arm comprises an imaging window fixed to a ring-actuator set-up described previously,[14,15] enabling loading and imaging from the same side. A preload was applied to each phantom using an upper brass plate, of larger surface area than the phantom, to ensure uniform contact between the phantom, the upper plate, and the imaging window (lower plate). The amount of preload required was dependent on the magnitude of variations in the surface topography in each phantom, which arose due to imperfections in the manual fabrication process of the phantoms, and typically ranged between 50 and 150 μm, as measured using OCT. The preload served to ensure optimal transfer of the load from the ring actuator during measurements.

The ring actuator introduced displacements of 80 to 120 nm to the sample surface using a square wave function at 5 Hz, synchronized to the OCT B-scan acquisition (at 10 Hz), as described in Ref. 15. This loading frequency was chosen to remain in the quasi-static loading regime, i.e., low enough to avoid wave propagation in the sample. The local displacement in the sample was measured by taking the phase difference between consecutive B-scans, i.e., between the compressed and uncompressed states. Displacement data were derived from the average of 50 sets of these B-scans. Temporal averaging served to reduce the variance of the measured displacement at each point and was performed in the complex plane in order to reduce systematic underestimation of displacement due to averaging of phase differences obtained at positions with low OCT signal-to-noise ratio (SNR).[37] The phase sensitivity of the system in a scanning configuration (calculated as the standard deviation of the measured phase difference between sequential B-scans of a stationary sample, over 50 pairs of B-scans) was 25 mrad at an OCT SNR of 50 dB, corresponding to a displacement sensitivity of 1.2 nm. Discrepancy between the measured sensitivity and the predicted shot noise–limited sensitivity (3.2 mrad at 50 dB)[38] is attributed to galvanometer lateral positioning error between B-scans.

The local strain in the sample was estimated from the measured displacements using a weighted-least squares (WLS) algorithm and represented in a strain elastogram. In WLS strain estimation, the measured displacement values are weighted based on the underlying OCT SNR at each point, since the phase variance and, therefore, the displacement measurement accuracy, depends on the OCT signal intensity. (We demonstrated in Ref. 15 that WLS strain estimation improves the strain sensitivity and DR over previously reported strain estimation techniques.) We applied Gaussian smoothing to the strain elastograms, using an 18×7-μm window (width $\times$ height) to further improve strain sensitivity. The axial strain resolution (axial distance over which the slope of axial displacement versus depth is calculated) was 90 pixels, corresponding to a physical length of 92 μm, using a group refractive index of 1.4. The lateral strain resolution was equal to the lateral resolution of the OCT system (11 μm).

3.3 *Finite Element Model*

3.3.1 *Model description*

FEMs of the compression OCE experiments were developed using the simulation software Abaqus (Dassault Systèmes, Providence, USA, version 6.10.1). To construct each model, a geometry was defined and material properties were assigned to deformable regions within the model. The geometry was then divided into discrete (finite) elements, in which an approximate solution to the governing equilibrium equations was determined, subject to the application of a known displacement along the boundary corresponding to the lower plate (imaging window) in the experiments. The solution provided the displacements, strains, and stresses on each of the finite elements.[39] The spacing of the elements (mesh size) ranged from 5 to 20 μm, with the finer mesh in areas where large variations in stress and strain

were expected, e.g., around inclusions. The model assumed linear elastic behavior of all materials.

An axisymmetric model was employed, in which a two-dimensional cross-sectional geometry was defined and then rotated about a central axis to obtain a 3-D visualization of the sample. This model yields an effective 3-D solution without the added computational complexity of solving the governing equations in three dimensions. Although inclusions were shaped as rectangular prisms in the experiments, rather than cylinders as in the axisymmetric model, measurements were made in a plane close to the center of the inclusions such that the measured deformation approximated that through the center plane of a cylinder.

3.3.2 *Determination of model inputs*

Inputs to the models of each experiment included:

- phantom geometry (total thickness, thickness of layers, inclusion dimensions, depth of inclusion below sample surface), as measured using OCT before application of preload;
- modulus contrast between features, determined from estimates of Young's modulus from the stress-strain curve of each silicone (further details below);
- amount of displacement introduced to the sample by the preload, as measured using OCT;
- amount of nanometer-scale displacement introduced to the sample surface by the actuator; and
- the friction conditions present in the experiment (further details below).

Compression testing of the bulk silicones typically revealed a nonlinear stress-strain relationship, as illustrated by the representative stress-strain curve in Fig. 2. However, as a relatively small range of strain (≤0.12) was used in OCE experiments, the silicones were modeled as linear elastic. The Young's modulus of each material was estimated based on the bulk strain due to the preload. For example, in an inclusion sample, the change in thickness of the matrix was measured from OCT images taken before and after preload, from which a bulk strain on the matrix

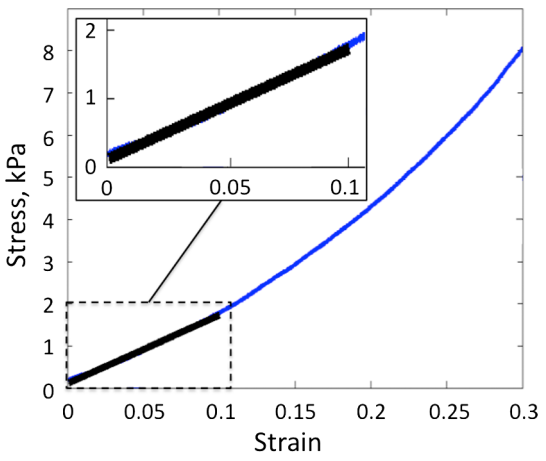

Fig. 2 Representative stress-strain curve obtained from compression testing of the silicones used in phantom fabrication. Inset shows an example of a linear fit (black line) used to estimate Young's modulus.

Table 1 Bulk mechanical characterization of silicone phantom materials.

Phantom number	Feature	Young's modulus (kPa)	Modulus contrast
1	Homogeneous	20	N/A
2	Bottom layer Top layer	520 14	37:1
3	Inclusion Matrix	837 19	45:1
4	Inclusion Matrix	153 15	10:1
5	Inclusion Matrix	100 20	5:1
6	Inclusion Matrix	34 17	2:1
7	Inclusion Matrix	20 19	1.1:1

was estimated. The Young's modulus was estimated by the linear regression from 0 to this bulk strain on the stress-strain curve of the matrix material (See Fig. 2). Similarly, the change in an inclusion thickness due to preload was determined and its modulus approximated using the same fitting procedure on the stress-strain curve of the inclusion material. This same procedure was used to estimate Young's modulus of the silicones in the bilayer phantom. Table 1 lists the estimated Young's modulus of each silicone as well as the modulus contrast between features (inclusion:matrix or bottom:top layer) for all phantoms used in this study.

Unless otherwise stated, the coefficients of friction used were 0.1 at the phantom-glass imaging window interface and 0.5 at the phantom-brass plate interface. These values were empirically determined to give the best quantitative matches between the modeled and measured displacements. The difference in the degree of friction between the upper and lower surfaces is expected, as the imaging window is smoother than the brass upper plate, and because silicone fluid (Wacker AK50) was applied to lubricate the phantom-imaging window interface. Exceptions to these conditions are specified, where relevant, in Secs. 4.1 and 4.2. Finally, a Poisson's ratio of 0.49 was assumed for all silicones.[40]

4 Results

4.1 *Comparison of Measured and Simulated Deformation in Compression OCE*

Figures 3(a)–3(c) present the structural OCT images, along with the measured and simulated displacement maps resulting from compression OCE experiments and FEMs, respectively, for (top to bottom) homogeneous, bilayer, and inclusion phantoms (Phantoms 1 to 3 in Table 1). Figure 3(d) is a comparison of the measured and simulated displacement versus depth taken from the positions indicated by the dashed lines in Figs. 3(b) and 3(c). Silicone fluid was used to lubricate the upper and lower surfaces to minimize friction, and these surfaces were

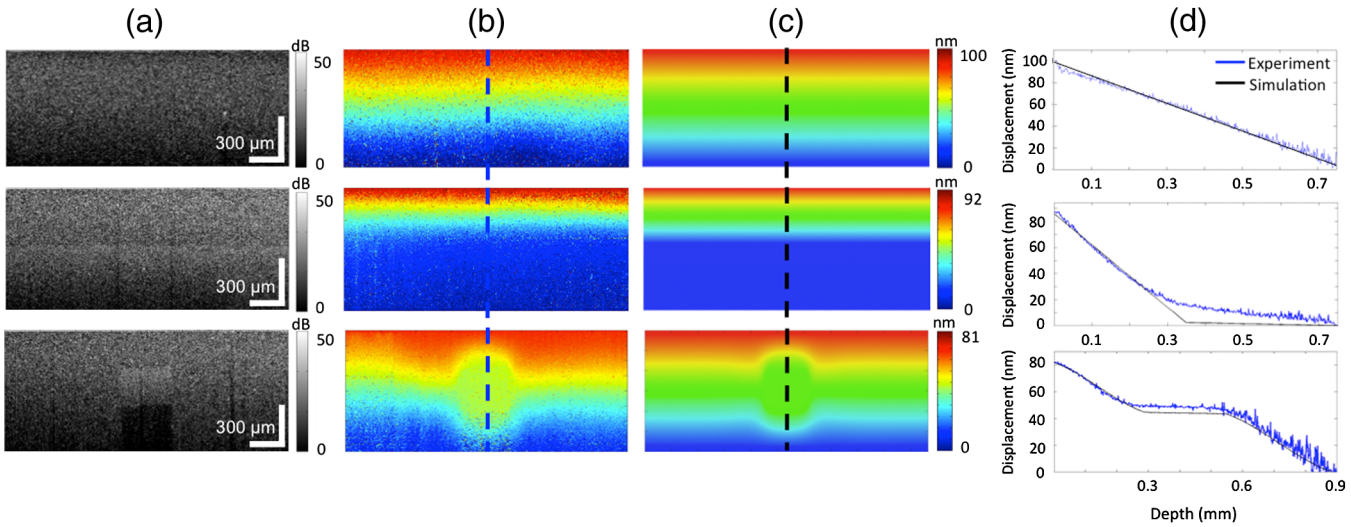

Fig. 3 Comparison of measured and simulated displacement maps in (top to bottom): homogeneous; bilayer; and inclusion phantoms. (a) OCT image; (b) experimentally measured displacement map; (c) simulated displacement map; and (d) displacement versus depth for the lateral positions indicated by the blue and black dashed lines in (b) and (c), respectively.

modeled as frictionless in the FEM, in order to simplify the mechanical system in the first instance.

Qualitatively, the measured and simulated displacement maps show good correspondence, and the displacement traces in Fig. 3(d) verify a good quantitative match. These traces also allow a clear interpretation of the displacement trends in each phantom. In each case, compression was introduced from the top of the image, resulting in maximum displacement at the top surface and zero displacement at the opposite surface, where the phantom was compressed against a rigid, unmoving plate. For the homogeneous case, a linear decrease in displacement with depth is observed, corresponding to a uniform local strain throughout the phantom.

In the bilayer phantom, two slopes are observed, with greater slope, corresponding to higher strain, in the softer top layer. The location of the change in slope corresponds to the physical interface between the layers. The slight discrepancy between the experiment and simulation in the displacement at the layer interface is likely to be due to an imperfect interface between the two silicone layers that arose during curing.

Finally, in the inclusion phantom, large displacement gradients, corresponding to higher strain, are observed in the matrix material, surrounding a region of bulk displacement, or low strain, in the stiff inclusion. The slight discrepancy in the displacement of the inclusion seen here is likely due to a slight discrepancy in the depth at which the inclusion was situated in the model versus in the actual phantom.

4.2 *Accuracy of Strain Elastograms in Representing Elasticity*

The agreement between measured and simulated displacement demonstrated in the previous section confirms the validity of the assumption of linear elastic behavior of these materials over the range of employed strains. In this section, we compare measured and simulated strain elastograms for varying geometries, friction conditions, and modulus contrasts. We also use FEMs to simulate the corresponding stress distributions and, thus, aid our analysis of mechanical artifacts in elastograms and their impact on accuracy.

4.2.1 *Nonuniform stress due to friction*

As described in Sec. 2.1, axial compression of a soft tissue sample is accompanied by lateral expansion (the Poisson effect). In the ideal case of zero friction between the sample and compressor, the sample is free to slip along this interface and expand laterally under axial compression. This is the case for the phantoms shown in Fig. 3, as the surfaces were well lubricated to minimize friction. When friction is present, this lateral expansion is restricted. This is illustrated in the plot of displacement versus depth, Fig. 4(a), for a homogeneous phantom in which no lubrication was used at the surfaces. The silicone used here, like many soft tissues, is inherently adhesive and is expected to undergo little or no slipping at the boundary in the absence of lubricant. In the experimental elastogram, Fig. 4(b), this restricted motion manifests as bands of low strain at the top and bottom surfaces, which are also seen in the simulated elastogram, Fig. 4(c), for which a no-slip condition was defined at the surfaces in the model.

The simulated stress, Fig. 4(d), reveals a nonuniform distribution, with increasing stress toward the center of the sample. This trend is attributed to the increasing restriction on lateral motion of the sample with distance from the free vertical edges.

4.2.2 *Nonuniform stress due to inhomogeneity*

Figure 5 presents the experimental and simulated elastograms, and simulated stress distribution of the same bilayer and inclusion phantoms presented in Sec. 4.1. The experimental strain elastograms were generated using the displacement maps in Figs. 3(c) and 3(d).

The elastograms of the bilayer phantom, Figs. 5(a) and 5(b), show layers of high and low strain, corresponding to the soft and stiff layers, respectively. Importantly, the stress distribution, Fig. 5(c), is uniform in this sample. There are no stress concentrations or strain artifacts apparent at the interface of the two materials. This confirms that the observed strain contrast should match the true modulus contrast between the layers as predicted by the mechanical analysis presented in Sec. 2.1.

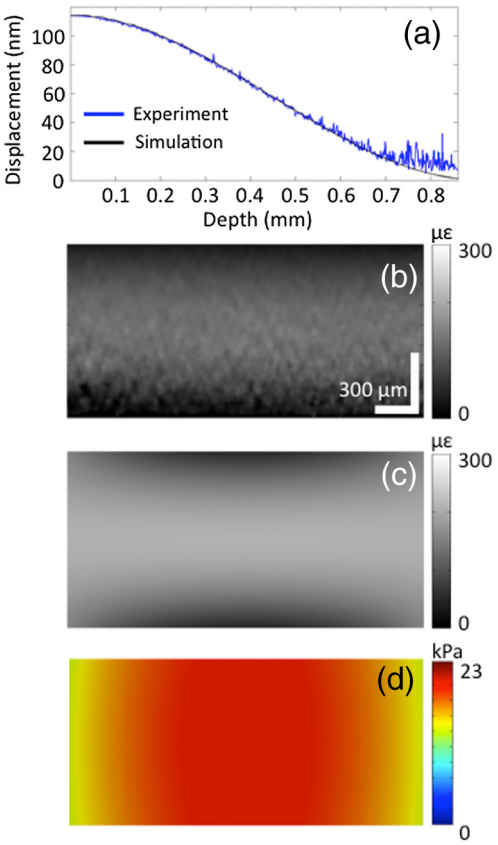

Fig. 4 Effect of friction on strain and stress distribution in a homogeneous sample. (a) Measured (blue) and simulated (black) displacement versus depth along the central vertical axis of the sample, (b) measured strain elastogram, (c) simulated strain elastogram, and (d) simulated stress map for a homogeneous sample with friction present at both surfaces.

In the elastograms of the inclusion phantom, Figs. 5(d) and 5(e), the stiff inclusion is clearly distinguishable as a region of very low strain, and higher strain is observed in the soft matrix. However, the strain in the matrix is not uniform throughout the elastogram even though this is a mechanically uniform material. This is due to variations in stress due to the presence of the stiff inclusion as seen in the simulated stress map in Fig. 5(f). Higher stresses above and below the inclusion manifest as regions of higher strain in the elastogram. In addition, at the vertical edges of the inclusion, a region of high stress is observed, adjacent to a region of lower stress in the matrix material. This can be attributed to a stress-shielding effect, in which the two materials at this location experience similar loads transferred from the material above, but the deformation of the matrix is restricted by that of the stiff inclusion. As the stress at this interface is not effectively distributed to the matrix, the inclusion experiences higher stress. This manifests in the elastograms as regions of low strain in the matrix adjacent to the sides of the inclusion.

As made apparent in Figs. 5(d) and 5(e), strain artifacts degrade the fidelity of the elastogram to the true distribution of modulus. The severity of these artifacts, however, depends on the modulus contrast between the inclusion and matrix. This is demonstrated in Fig. 6, where the modeled stress and strain are shown for Phantoms 3 to 7 listed in Table 1, from highest to lowest modulus contrast (top to bottom). Note that the color scale for the stress maps was adjusted in each case, depending on the preload strain applied to the sample, to facilitate comparison of stress distribution due solely to changes in modulus contrast. The inclusion sizes in each set of images in Fig. 6 correspond to those used in the actual experiments (in the range of 300 to 500 μm in height and width); however, recall that the resulting strain contrast is independent of the inclusion size [Eq. (1)]. This sequence of images illustrates that although the stress concentrations and strain artifacts decrease

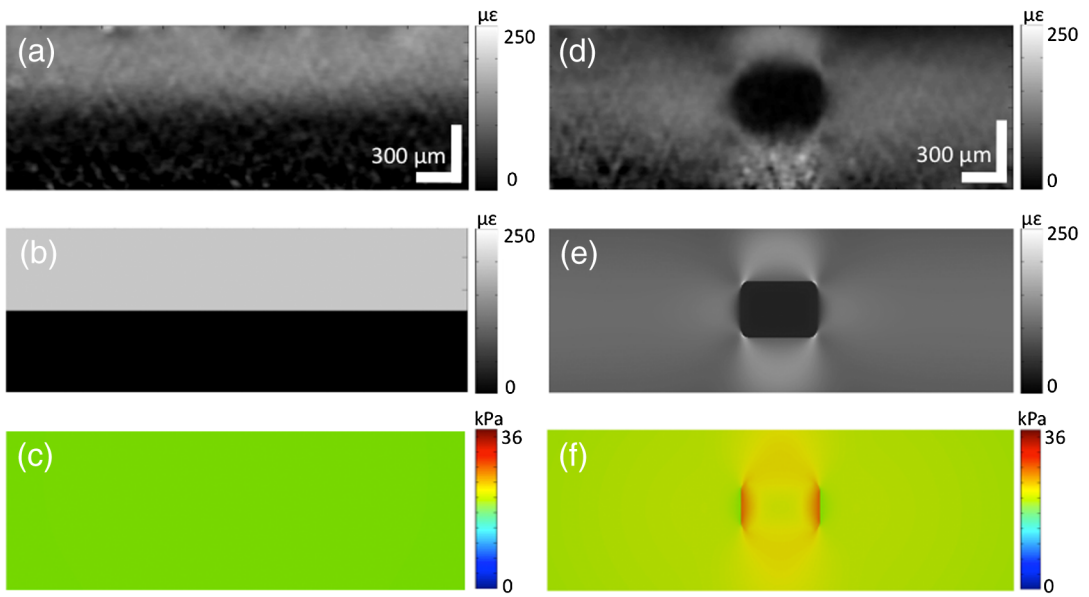

Fig. 5 Measured strain elastogram, simulated strain elastogram, and simulated stress map, respectively, for (a)–(c) a bi-layer sample with modulus contrast 37:1 and (d)–(f) an inclusion sample with modulus contrast 45:1.

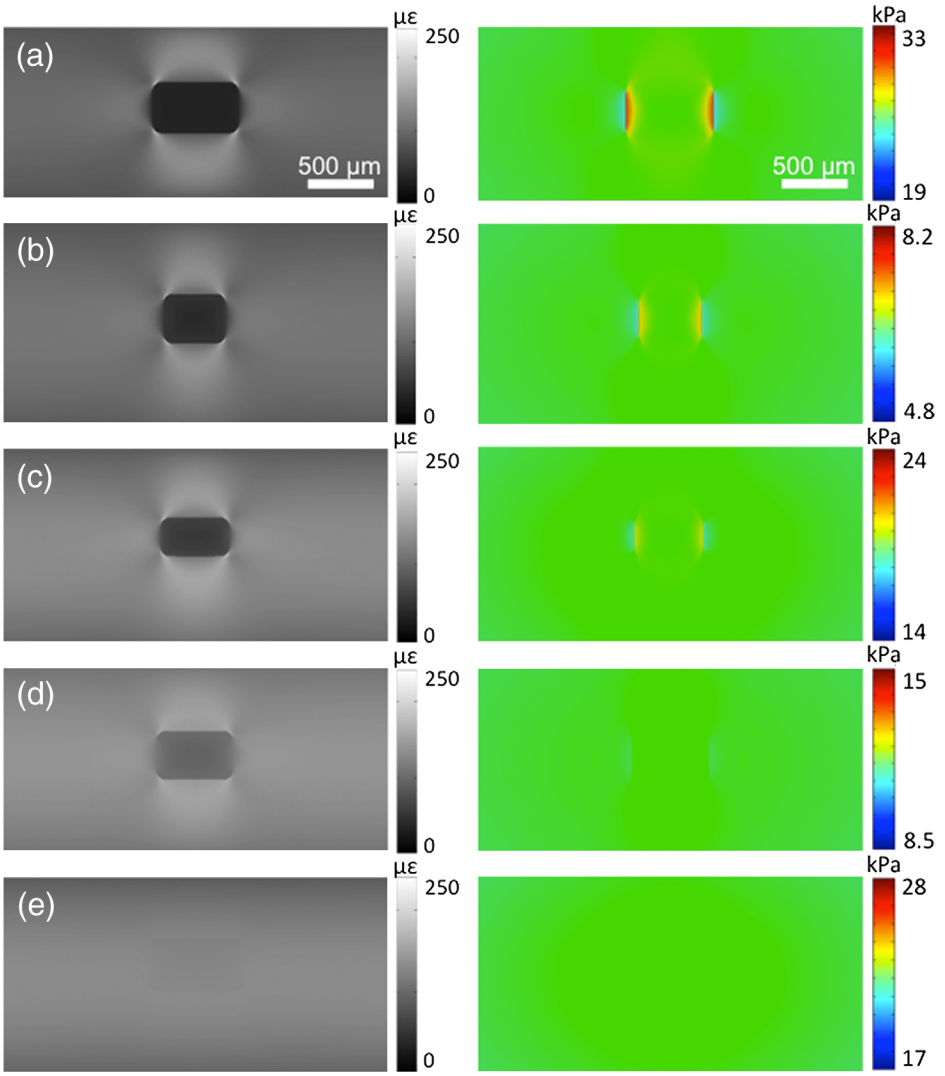

Fig. 6 Simulated strain elastograms and stress maps for varying degrees of contrast between inclusion and matrix. Modulus contrasts (inclusion:matrix): (a) 45:1, (b) 10:1, (c) 5:1, (d) 2:1, (e) 1.1:1.

with decreasing modulus contrast, the contrast between inclusion and background in the elastogram also diminishes. In the following sections, we consider the limits on this contrast imposed by both mechanical and imaging parameters.

4.2.3 *Contrast transfer efficiency*

Figure 7 compares, using Eq. (1), the true modulus contrast, C_t, and predicted strain contrast, C_o, to the strain contrast observed between the inclusion and matrix in the OCE experiments. The curve for the predicted strain contrast was generated for a Poisson's ratio of 0.49. The average strains in the elastograms were calculated for regions both within the inclusion and in the matrix at least 500 μm away from the inclusion. Fifty strain pixels were used to calculate the average and standard deviation of strain in each feature, all at the same depth in the sample to minimize the effects of decreasing OCT SNR with depth on the standard deviation of strain. Error bars reflect the standard deviation of contrast between the inclusion and matrix. The contrast values are plotted as amplitude ratios on a logarithmic scale, $C_o(\mathrm{dB}) = 20\log(\varepsilon_{\mathrm{inclusion}}/\varepsilon_{\mathrm{matrix}})$, following

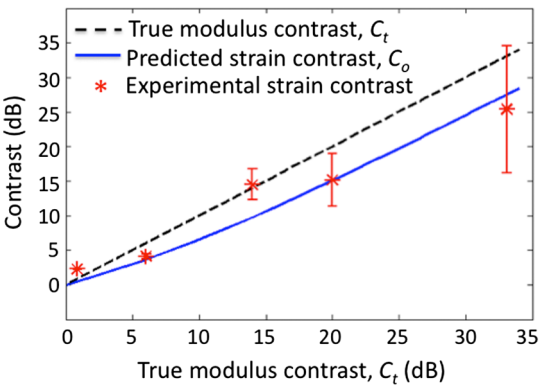

Fig. 7 True modulus contrast, C_t (black dashed line), predicted strain contrast, C_o (blue solid line) from Eq. (1), and experimental strain contrast versus true modulus contrast for a stiff inclusion in a soft matrix. All contrasts are plotted on a 20 log scale.

the convention used in ultrasound elastography studies of contrast.[32,34,41,42]

Note that for modulus contrasts >10:1 (20 dB), the observed contrast maintains an approximately constant offset of ~6 dB from the true modulus contrast. In other words, the CTE reaches a maximum of just over 0.5 for modulus contrasts of 10:1 and greater. This can be explained by considering the interaction of the inclusion and matrix under compression. A stiff inclusion resists deformation, and because it is mechanically coupled to the surrounding matrix, this causes a perturbation to the stress and strain in the matrix. This manifests as stress and strain concentrations, as illustrated in Figs. 5 and 6. Increasing inclusion modulus increases these perturbations on the matrix, also illustrated in Fig. 6. Above a certain contrast, the inclusion can be regarded as a rigid body, i.e., it undergoes very little strain; thus, the perturbations it causes to the matrix remain fixed regardless of increases in modulus contrast.[32] Low contrast inclusions, which more easily deform with the matrix under compression and cause little perturbation on the matrix strain, will result in strain elastograms that more accurately represent the true mechanical contrast. This reiterates that a fundamental limitation on strain elastogram accuracy, previously described in Refs. 32 and 34, also applies to OCE.

4.3 *Sensitivity of Strain Elastograms to Variations in Elasticity*

The CTE limits the accuracy of mechanical contrast in strain elastograms, but to determine the smallest detectable mechanical contrast, i.e., the elastogram sensitivity, we must consider the limitations of the employed imaging system and strain estimation process. Using the definitions for elastogram performance parameters presented in Sec. 2.2, we can estimate the strain sensitivity (S_ε) and DR for the measurements performed in this article. These values are summarized in Table 2. Note that these values are specific to the phase stability (25 mrad) and wavelength (835 nm) of the employed OCT system, the axial strain resolution (92 μm), and the strain estimation technique (WLS with Gaussian smoothing).

The reported strain DR of 56 dB is based on a theoretical maximum displacement corresponding to a phase change of π radians within one strain resolution (in this case, 1600 $\mu\varepsilon$ over 92 μm). However, the actual maximum displacement used in the experiments corresponded to a phase change of π radians over the entire depth of the phantom (~1 mm) to avoid the need for any phase unwrapping. This decreases the actual strain DR for these measurements to ~36 dB and points to the potential improvement to be gained in the strain DR through implementation of robust phase unwrapping algorithms.

S_ε was calculated as the standard deviation of 500 strain pixel values over a 50 × 600 μm region in an elastogram of a homogeneous phantom, and at a depth with an average OCT SNR of 20 dB. S_ε degrades with decreasing OCT SNR. For example, in the same phantom, S_ε of 3.7 and 5.6 $\mu\varepsilon$ was calculated at depths of average OCT SNR of 12 and 8 dB, respectively. S_ε also depends on the strain axial resolution and is expected to improve with a tradeoff of lower resolution.[15]

Table 2 Estimated elastogram performance parameters (dB calculated using 20 log).

ε_{max}	1600 $\mu\varepsilon$ (−56 dB)
ε_{min} (S_ε)	2.4 $\mu\varepsilon$ (−112 dB)
DR_ε	667 (56 dB)

S_ε limits the minimum detectable contrast in strain elastograms, i.e., to distinguish two features in a strain elastogram, the difference in strain between two features must be greater than S_ε. Figure 8 illustrates this problem of feature detectability. In Figs. 8(a)–8(c), experimental elastograms of inclusion phantoms with decreasing modulus contrast are shown, along with plots, Fig. 8(d), of the simulated (solid lines) and experimental (dotted lines) strain values through the locations indicated by the dashed lines in the elastograms. This plot illustrates the degradation of strain contrast due to noise in the experimental versus simulated strain. Still, the inclusions are readily detectable in each elastogram, including the inclusion with small modulus contrast of 1.1:1, Fig. 8(c). The measured strains in the inclusion and matrix for this phantom were 90 and 120 $\mu\varepsilon$, respectively, a difference sufficiently greater than the strain sensitivity to make the inclusion readily detectable.

The strain sensitivity, in combination with the CTE of a particular geometry, ultimately determines the sensitivity to variations in elasticity. For layered samples, as well as for inclusion samples with low modulus contrast between the inclusion and matrix, such as that in Fig. 8(c), the strain contrast closely approximates modulus contrast (CTE close to 1). It follows that the strain sensitivity is approximately equal to the modulus

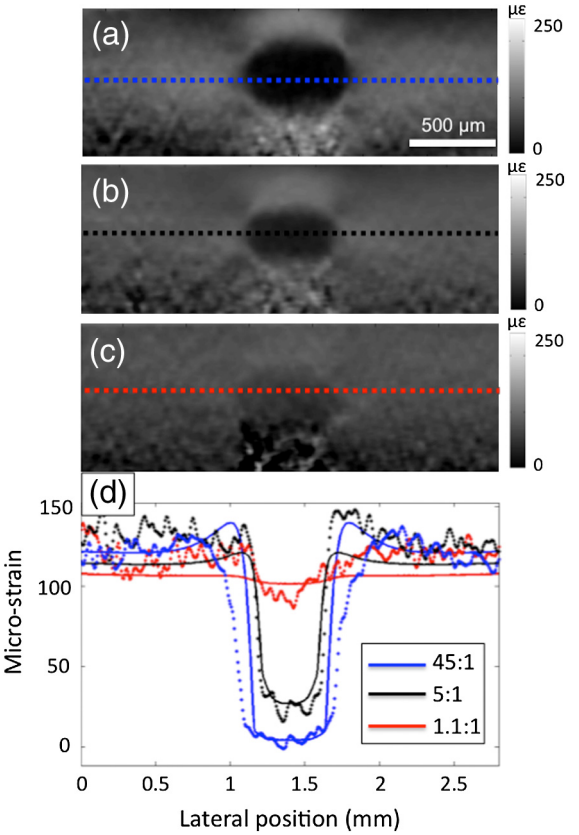

Fig. 8 Impact of strain sensitivity on detectable contrast. Experimental strain elastograms for modulus contrasts (a) 45:1, (b) 5:1, and (c) 1.1:1. (d) Plots of experimental (dotted lines) and simulated (solid lines) strain in the samples at depths specified by the dashed lines in the elastograms.

sensitivity in these cases. Considering our best-case scenario, with S_e of 2.4 $\mu\varepsilon$ and maximum strain of 1600 $\mu\varepsilon$, a modulus contrast of $\varepsilon_{max}/(\varepsilon_{max} - S_e)$, corresponding to ~1.002:1, could theoretically be detected in a strain elastogram. In the phantoms shown in Fig. 8, where the matrix material has Young's modulus ~18 kPa, this would translate to the ability to detect a change in elasticity as small as 36 Pa.

5 Discussion

The measurements and simulations presented here aid in the understanding of mechanical contrast by illustrating the limitations imposed by sample mechanics and the image formation process. In the field of ultrasound elastography, several studies have investigated the combined impact of mechanics and imaging on the resulting contrast in strain elastograms.[32–34] However, there are some key differences in the limits on contrast at the scale of OCE.

First, a consideration specific to OCE highlighted in this work is the importance of mechanical conditions at the sample surface, as elastograms in OCE are limited to the first 1 to 2 mm of tissue. In compression OCE, in particular, friction decreases the amount of axial strain, hence, increasing the apparent stiffness of the material. It also introduces surface artifacts in strain elastograms, such as those in Figs. 4(b) and 4(c), which could potentially be misinterpreted as regions of higher Young's modulus in what is actually a mechanically homogeneous sample. For a thick sample, this band of low strain could potentially dominate the entire OCE field of view. Even in noncontact OCE techniques where such friction is absent, such as those that use laser pulse[22] or air puff excitation,[9] an uneven sample surface, such as that expected to manifest in tissue, can induce complex motion and is expected to cause simple models of mechanical behavior to break down. The importance of such surface effects represents an added challenge in advancing OCE techniques toward practical clinical use.

Second, the displacement sensitivity of OCT, especially using phase-sensitive detection, results in a very high sensitivity to changes in tissue elasticity. Although the DR of strain for compression OCE found in this article is similar to that reported for compression elastography using ultrasound,[42] the microstrain sensitivity of OCE should enable detection of more subtle increments in tissue elasticity, as illustrated in Sec. 4.3.2. Together with the high spatial resolution of OCE, this suggests the potential to differentiate tissues within an elastogram that may not be distinguishable with the sensitivity of ultrasound and magnetic resonance (MR) elastography. This has important implications for providing mechanical contrast between, for example, healthy, premalignant, and malignant tissues of the breast, which have been reported to exhibit elasticity values in the narrow range of 0.2 to 2 kPa, as measured by atomic force microscopy.[43]

The capacity to detect the mechanical heterogeneity in tissue will also vary depending on the spatial scale being probed. The scale of tissue probed by ultrasound and MR elastography is closer to that probed by manual palpation but with the important advantage of being able to probe deep within the body. On the other hand, OCE should be able to resolve mechanical heterogeneity on a finer length scale but within a smaller field of view. An indication of the impact of spatial resolution on detectable mechanical contrast is seen in the elastograms of the inclusion phantom in Figs. 5(d) and 5(e). The lower axial strain resolution (92 μm) employed in the experiment, compared to the element spacing used in the FEM (10 μm), tends to blur the true edges of the inclusion in the experimental elastogram. This also accounts for the absence of very localized variations in strain in the experiment versus the simulation, e.g., small points of high strain visible at the corners of the inclusion in the simulation are not resolved in the experiment. A study of the impact of spatial resolution on mechanical contrast is beyond the scope of this current work, but such an investigation would provide additional insight into the unique tissue contrast OCE can offer.

A limitation of the present study was the simplification of the response of nonlinear materials to a linear elastic model of behavior. However, we took account of the nonlinearity of the materials by estimating their effective Young's moduli based on bulk strain due to preload. Input of this effective Young's modulus into a linear elastic FEM gave similar results to input of the stress-strain curve into a nonlinear FEM. Thus, we chose to use only linear elastic models to simplify the mechanical analysis in this study. Furthermore, all linear fits to the stress-strain curves to estimate modulus had an error ≤95 Pa, which is on the order of our modulus sensitivity for these materials, so this error had negligible impact on the final comparison of elastogram contrast to "true" contrast. However, there was some uncertainty in the estimation of bulk strain of each phantom, as we assumed that the bulk strain measured in the imaging plane (B-scans) was representative of the bulk strain of the matrix and inclusions out of the plane. The asymmetry of the inclusions (~50 μm tolerance was achievable in cutting each face of the inclusion) could have resulted in a discrepancy between the actual effective modulus of each silicone and the calculated "true" modulus. This explanation most likely accounts for discrepancies between the observed strain contrast in elastograms and the strain contrast predicted by the CTE in Fig. 7.

Unlike the silicones used here, it has been found that many tissues more closely follow linear behavior at such low strains.[29] In applications of OCE where high strains (>0.1) may be difficult to avoid, such as in arterial tissues, models for elastogram reconstruction that incorporate tissue nonlinearity have been proposed.[44]

The qualitative nature of strain elastograms was demonstrated in several cases in this article through the presence of geometry- and contrast-dependent strain artifacts. The CTE was used to quantify the impact of these artifacts on elastogram accuracy. For the particular geometry of an inclusion in a matrix, it is feasible that, for a given value of Poisson's ratio, a correction factor could be applied, based on Eq. (1), to quantify the true modulus contrast from a strain elastogram. However, while it provides a suitable first approximation of an inhomogeneous tissue structure for the purposes of this study, this simplistic inclusion geometry and the contrast transfer function derived for it are not expected to accurately represent the much more complex microstructure found in tissue. Thus, in tissue, we can expect a degradation of the CTE with higher modulus contrast between adjacent tissues, i.e., with a higher degree of stress nonuniformity.

Quantitative estimation of modulus distribution using compression OCE will require implementation of more advanced methods, such as approaching elastogram reconstruction as an inverse problem. Avenues toward quantitative OCE using inverse methods have been proposed, including a model-based approach, in which an analytical or numerical model (such as FEM) is used to iteratively reconstruct a quantitative modulus image.[7,44,45] More recent studies have moved toward quantification of modulus by implementing transient loading

techniques in which modulus may be extracted directly from the velocity of shear waves or surface waves in the sample.[10,19–21] However, these techniques come at a loss of resolution, as they assume tissue homogeneity for the length over which the shear wave speed is calculated. This assumption may not be suitable for imaging organs with heterogeneous, complex structures, such as the breast.

Despite currently providing only relative measurements, compression OCE is expected to remain an attractive technique for clinical translation, as it is relatively straightforward and practical to implement and provides higher spatial resolution than other OCE techniques. Furthermore, the relative mechanical contrast in strain elastograms may often be sufficient for detecting variations due to changes in tissue pathology, especially for clinical applications focused on detecting the boundaries of diseased tissue, where both diseased and healthy tissue lie within the imaging field of view.

The analysis presented here provides a framework for evaluation of the sensitivity and accuracy of contrast in other OCE techniques. Finite element modeling is expected to be an essential tool for testing the validity of assumptions made about sample behavior in various OCE techniques and for analyzing how variables such as geometry, surface conditions, loading rate, and detection schemes impact on contrast.

6 Conclusion

We have performed an evaluation of mechanical contrast in strain elastograms produced using phase-sensitive compression OCE, highlighting the limitations imposed by mechanical deformation and by imaging system noise and signal processing parameters. We have illustrated these limitations by presenting experimental and simulated elastograms of tissue-mimicking phantoms with a range of mechanical properties. Based on our analysis, we summarize the following answers to the questions proposed in the introduction as they apply to compression OCE:

1. How accurately do OCE elastograms represent the elasticity distribution within a sample?

   - Layered structures and structures with low elasticity contrast tend toward uniform stress and high accuracy (CTE $\sim$ 1).
   - Structures with high elasticity contrast and/or surface friction have nonuniform stress and lower accuracy (CTE < 1).
   - For an inclusion geometry, CTE plateaus at 0.5 for elasticity contrast >10:1.

2. What is the sensitivity of OCE elastograms to variations in elasticity within a sample?

   - For our imaging and strain estimation parameters, we were able to measure an elasticity contrast of 1.1:1 and predicted a maximum sensitivity to elasticity contrast of 1.002:1.

3. What factors limit elastogram accuracy and sensitivity?

   - Mechanical factors: geometry, friction, elasticity contrast between features.
   - Imaging factors: displacement sensitivity, resolution, strain estimation parameters.

Despite mechanical artifacts limiting compression OCE to providing relative measurements of elasticity, the microstrain sensitivity demonstrated here, together with its high spatial resolution, has not previously been attainable by other methods. Access to this new regime for tissue mechanical measurements suggests that phase-sensitive compression OCE is a very promising technique for providing novel and clinically meaningful tissue contrast.

Acknowledgments

We thank Robert Day at Royal Perth Hospital Department of Medical Physics for his assistance with Instron measurements and Martin Bruetsch of Wacker Silicones for providing silicone materials and expertise. K. M. K. is supported by the Scholarship for International Research Fees, UWA and B. F. K. by the Raine Medical Research Foundation.

References

1. J. F. Greenleaf, M. Fatemi, and M. Insana, "Selected methods for imaging elastic properties of biological tissues," *Annu. Rev. Biomed. Eng.* **5**(1), 57–78 (2003).
2. J. M. Schmitt, "OCT elastography: imaging microscopic deformation and strain of tissue," *Opt. Express* **3**(6), 199–211 (1998).
3. R. Righetti, S. Srinivasan, and J. Ophir, "Lateral resolution in elastography," *Ultrasound Med. Biol.* **29**(5), 695–704 (2003).
4. A. Manduca et al., "Magnetic resonance elastography: non-invasive mapping of tissue elasticity," *Med. Image Anal.* **5**(4), 237–254 (2001).
5. E. K. Dimitriadis et al., "Determination of elastic moduli of thin layers of soft material using the atomic force microscope," *Biophys. J.* **82**(5), 2798–2810 (2002).
6. J. Guck et al., "Optical deformability as an inherent cell marker for testing malignant transformation and metastatic competence," *Biophys. J.* **88**(5), 3689–3698 (2005).
7. A. S. Khalil et al., "Tissue elasticity estimation with optical coherence elastography: toward mechanical characterization of *in vivo* soft tissue," *Ann. Biomed. Eng.* **33**(11), 1631–1639 (2005).
8. W. Qi et al., "Phase-resolved acoustic radiation force optical coherence elastography," *J. Biomed. Opt.* **17**(11), 110505–110505 (2012).
9. S. Wang et al., "Noncontact measurement of elasticity for the detection of soft-tissue tumors using phase-sensitive optical coherence tomography combined with a focused air-puff system," *Opt. Lett.* **37**(24), 5184–5186 (2012).
10. R. K. Manapuram et al., "*In vivo* estimation of elastic wave parameters using phase-stabilized swept source optical coherence elastography," *J. Biomed. Opt.* **17**(10), 100501–100503 (2012).
11. M. R. Ford et al., "Method for optical coherence elastography of the cornea," *J. Biomed. Opt.* **16**(1), 016005–016007 (2011).
12. C. Li et al., "Noncontact all-optical measurement of corneal elasticity," *Opt. Lett.* **37**(10), 1625–1627 (2012).
13. S. G. Adie et al., "Audio frequency *in vivo* optical coherence elastography," *Phys. Med. Biol.* **54**(10), 3129–3139 (2009).
14. B. F. Kennedy et al., "*In vivo* dynamic optical coherence elastography using a ring actuator," *Opt. Express* **17**(24), 21762–21772 (2009).
15. B. F. Kennedy et al., "Strain estimation in phase-sensitive optical coherence elastography," *Biomed. Opt. Express* **3**(8), 1865–1879 (2012).
16. B. F. Kennedy et al., "*In vivo* three-dimensional optical coherence elastography," *Opt. Express* **19**(7), 6623–6634 (2011).
17. K. M. Kennedy et al., "Needle optical coherence elastography for tissue boundary detection," *Opt. Lett.* **37**(12), 2310–2312 (2012).
18. A. Nahas et al., "3D static elastography at the micrometer scale using Full Field OCT," *Biomed. Opt. Express* **4**(10), 2138–2149 (2013).
19. X. Liang et al., "Acoustomotive optical coherence elastography for measuring material mechanical properties," *Opt. Lett.* **34**(19), 2894–2896 (2009).

20. M. Razani et al., "Feasibility of optical coherence elastography measurements of shear wave propagation in homogeneous tissue equivalent phantoms," *Biomed. Opt. Express* **3**(5), 972–980 (2012).
21. C. Li et al., "Quantitative elastography provided by surface acoustic waves measured by phase-sensitive optical coherence tomography," *Opt. Lett.* **37**(4), 722–724 (2012).
22. K. D. Mohan and A. L. Oldenburg, "Elastography of soft materials and tissues by holographic imaging of surface acoustic waves," *Opt. Express* **20**(17), 18887–18897 (2012).
23. B. S. Garra et al., "Elastography of breast lesions: initial clinical results," *Radiology* **202**(1), 79–86 (1997).
24. A. Grimwood et al., "Elastographic contrast generation in optical coherence tomography from a localized shear stress," *Phys. Med. Biol.* **55**(5515), 5515–5528 (2010).
25. V. Crecea et al., "Magnetomotive nanoparticle transducers for optical rheology of viscoelastic materials," *Opt. Express* **17**(25), 23114–23122 (2009).
26. R. K. Wang, Z. Ma, and S. J. Kirkpatrick, "Tissue Doppler optical coherence elastography for real time strain rate and strain mapping of soft tissue," *Appl. Phys. Lett.* **89**(14), 144103 (2006).
27. B. F. Kennedy et al., "Improved measurement of vibration amplitude in dynamic optical coherence elastography," *Biomed. Opt. Express* **3**(12), 3138–3152 (2012).
28. E. Konofagou and J. Ophir, "A new elastographic method for estimation and imaging of lateral displacements, lateral strains, corrected axial strains and Poisson's ratios in tissues," *Ultrasound Med. Biol.* **24**(8), 1183–1199 (1998).
29. T. A. Krouskop et al., "Elastic moduli of breast and prostate tissues under compression," *Ultrasonic Imaging* **20**(4), 260–274 (1998).
30. W. C. Yeh et al., "Elastic modulus measurements of human liver and correlation with pathology," *Ultrasound Med. Biol.* **28**(4), 467–474 (2002).
31. H. Huang et al., "The impact of calcification on the biomechanical stability of atherosclerotic plaques," *Circulation* **103**(8), 1051–1056 (2001).
32. H. Ponnekanti et al., "Fundamental mechanical limitations on the visualization of elasticity contrast in elastography," *Ultrasound Med. Biol.* **21**(4), 533–543 (1995).
33. I. Céspedes and J. Ophir, "Reduction of image noise in elastography," *Ultrasonic Imaging* **15**(2), 89–102 (1993).
34. F. Kallel, M. Bertrand, and J. Ophir, "Fundamental limitations on the contrast-transfer efficiency in elastography: an analytic study," *Ultrasound Med. Biol.* **22**(4), 463–470 (1996).
35. G. Lamouche et al., "Review of tissue simulating phantoms with controllable optical, mechanical and structural properties for use in optical coherence tomography," *Biomed. Opt. Express* **3**(6), 1381–1398 (2012).
36. A. Curatolo, B. F. Kennedy, and D. D. Sampson, "Structured three-dimensional optical phantom for optical coherence tomography," *Opt. Express* **19**(20), 19480–19485 (2011).
37. A. Szkulmowska et al., "Phase-resolved Doppler optical coherence tomography—limitations and improvements," *Opt. Lett.* **33**(13), 1425–1427 (2008).
38. M. A. Choma et al., "Spectral-domain phase microscopy," *Opt. Lett.* **30**(10), 1162–1164 (2005).
39. K.-J. Bathe, *Finite Element Procedures*, Prentice Hall Englewood Cliffs, New Jersey (1996).
40. J. Ilg et al., "Determination of dynamic material properties of silicone rubber using one-point measurements and finite element simulations," *IEEE Trans. Inst. Meas.* **61**(11), 3031–3138 (2012).
41. N. Belaid et al., "Lesion detection in simulated elastographic and echographic images: a psychophysical study," *Ultrasound Med. Biol.* **20**(9), 877–891 (1994).
42. T. Varghese and J. Ophir, "A theoretical framework for performance characterization of elastography: the strain filter," *IEEE Trans. Ultrson. Ferr.* **44**(1), 164–172 (1997).
43. M. Plodinec et al., "The nanomechanical signature of breast cancer," *Nat. Nanotechnol.* **7**(11), 757–765 (2012).
44. R. Karimi et al., "Estimation of nonlinear mechanical properties of vascular tissues via elastography," *Cardiovasc. Eng.* **8**(4), 191–202 (2008).
45. A. H. Chau et al., "Mechanical analysis of atherosclerotic plaques based on optical coherence tomography," *Ann. Biomed. Eng.* **32**(11), 1494–1503 (2004).